Experimental and numerical study of thermal and mechanical properties of porous materials based on triply periodic surfaces

Anton V. Eremin[1], Mikhail A. Frolov[2], Alexander F. Krutov[2,3], Mikhail I. Smolkov[2,3], Dmitry M. Bragin[1], Andrey I. Popov[1]

[1] *Heat Power Department, Samara State Technical University, 443100 Samara, Russia.*

[2] *Samara Center for Theoretical Materials Science, Samara State Technical University, 443100 Samara, Russia.*

[3] *Research Laboratory of Computational Geometry and Theoretical Materials Science, Povolzhskiy State University of Telecommunications and Informatics, Samara, 443010, Russia.*

✉ Corresponding author.

E-mail: m.smolkov97@gmail.com

ABSTRACT

We have generated 3D models of porous structures based on eight triply periodic surfaces (TPSs) and studied their thermal and mechanical properties. The TPSs were derived from topological network representation of zeolite crystal structures by a previously developed method. The resulting TPSs correspond to P, C(P) and IW-P topological types. We have developed software for the preparation of the TPS models for 3D printing, simulated the corresponding porous materials, and computed their physical properties. We have manufactured porous materials for three TPSs by 3D printing with styrene butadiene styrene and polyamide PA-12. PA-12 samples were formed from liquid phase and their

solidification occurs under UV radiation. Thermal and mechanical properties of manufactured samples were studied numerically and experimentally. The results of the modeling were found in good agreement with the experiment.

KEYWORDS

triply periodic surfaces, porous material, additive manufacturing, thermal conductivity, compression stiffness.

1 Introduction

Macroscopic cellular and porous structures with pores and cells of different types and sizes have received much attention in modern material science and engineering applications [1]. Ordered porous structures obtained on the basis of smooth triply periodic surfaces (TPS) including minimal surfaces (TPMS) with sufficiently complex and different topological and geometrical structures form a separate class among them [2–4]. This class of porous structures possess non trivial thermal-insulating, vibration-isolating, mechanical and other physical properties whereby they became the objects of intense theoretical and experimental studies [5–14]. Notice that it is possible to construct new composites and metamaterials on the basis of these structures by filling the pores with materials showed the necessary properties different from ones of the frame material [11]. The development of additive manufacturing (AM) technology in recent years given new impulse to study the structures obtained from TPS [8,10]. AM allows the production of thin-walled products with complex topological types and geometrical shapes. This is achieved with layer-by-layer solidification at optimal conditions for specific materials, as a result, this enables lower shrinkage of the sample. At the same time the current utilization of TPSs for the development of porous structures is limited to a small number of TPSs suitable for AM, thus emphasizing the importance of generating new TPSs [15]. Recently [16–19], we proposed a novel approach for creating TPSs and corresponding porous structures based on a

topological description of atom networks of the natural crystals in particular zeolites. In fact, our method gives the possibility to obtain unlimited quantity of different TPSs from periodic network templates by the ToposPro software package [20]. If a finite thickness is given to the generated surface, it can be produced by AM technology and its mechanical properties can be studied experimentally or estimated in the most common software packages like ANSYS [21]. Several recent studies have also focused on creating new TPS/TPMSs [23–27]. In particular, another method, which uses the ToposPro package was proposed to simulate porous space [23]. In this method, a TPS is constructed as a surface of equal electron density in atom lattice of some crystal which is calculated in DFT approach. Due to this the method involves optimizing the atomic structure for DFT calculations and thus requires a lot of computer time. Note that developed by us method, which is purely based on geometric and topological properties of a periodic network, works on arbitrary periodic frameworks and hence can be adapted both for natural crystals and of any mathematically generated networks [26] as templates. One more method for generating porous structures uses Voronoi diagrams and Delaunay triangulations [24], but it is limited to disordered two-dimensional structures, while our approach produces ordered 3D porous structures. Known TPMSs can also be used to generate porous materials [25,27] but in this case, minimal surfaces must be specified by analytical formulas, and the minimality of the resulting structures is not always guaranteed [25]. In the present work, we produced eight models of porous structures from various zeolite Crystals [22]: Sodalite (SOD), Rhodonite (RHO), Linde Type A (LTA), Mg-BCCT (BCT), STA-6 (SAS), Merlinoite (MER), MAPO-39 (ATN), CoAPO-CJ62 (JSW). The zeolite-based structures generated varied by topological type, genus, spatial groups, topology of labyrinth nets, Hopf?s nets topology, and balance properties. The choice of zeolites and the corresponding TPS in this work was conditioned by the problem of establishing correlations between the topological features of the surface and its thermal and mechanical properties. We have developed software for the preparation of the TPS models for 3D printing, simulated the corresponding porous structures, and computed their physical properties. Further, we created 3D printed samples of different

shapes and sizes using SBS filament and PA-12 polyamide for three zeolite-based structures (SOD, MER and JSW). At the next stage, we studied thermal properties of the obtained new structures, in particular, temperature fields, heat flow fields and effective thermal conductivity coefficients. An experimental investigation of the samples obtained by 3D printing methods was also carried out. Experimental measurements of the thermophysical properties were shown to be in good agreement with the theoretical calculations. Along with the thermophysical properties, the mechanical parameters of cuboid porous samples from PA-12 were measured and their good agreement with values calculated in the ANSYS software was founded. The structure of the paper is as follows. In Section 2 the method for generating triply periodic nets using the ToposPro program package and the technique for the construction of porous structures based on these nets in a format available for additive manufacturing are described shortly. Section 3 is devoted to numerical modeling of thermal properties for the discussed in the paper porous structures as well as the experimental verification of used numerical models. In Section 4 the numerical modeling and experimental measurement of mechanical properties are discussed. In the Conclusion the main results of the work are summarized.

2 Generation of porous materials from TPS derived from atomic nets of crystals

In this paper, the procedure for generation of porous structures from TPS is implemented into a software package based on a new network approach for generating triply periodic surfaces from crystal structures of chemical compounds [18]. This approach which was implemented in ToposPro package includes these consecutive steps:

(i) Firstly, using universal Domains algorithm [28] (Fig. 1 left) a periodic net is constructed for a given crystal structure.

(ii) Secondly, a natural tiling for obtained periodic net is generated [29]. The aforementioned tiling comprises polyhedral cages, referred to as natural tiles, that are surrounded by periodic nets' rings (natural tile faces) and designated by face symbols [A^x , B^y , C^z , . . .], where *A*, *B*, *C*, . . . are sizes of

the rings and *x*, *y*, *z*, . . . are numbers of the rings of a given size in the tile. Symmetry-independent rings of a particular size *A* are designated *Aa*, *Ab*, *Ac*, . . . (Fig. 1 middle). The inherent characteristic of natural tiles is their role as fundamental (minimal) cages from which any other cage can be constructed by combining multiple natural tiles.

(iii) Finally, creating TPSs through the process of enumerating all possible ways of eliminating natural tile faces from the initial tiling, while ensuring that the set of remaining faces adheres to three specific conditions:

(a) decoration condition mandates that all vertices and edges must be positioned on the TPS;

(b) edge condition which requires that any edge of the net is shared by strictly two faces from the set;

(c) vertex condition is used to make sure that all edges having a common vertex belong to different pairs of faces. These conditions allow the resulting series of faces to form a single TPS without self-intersections (Fig. 1 right).

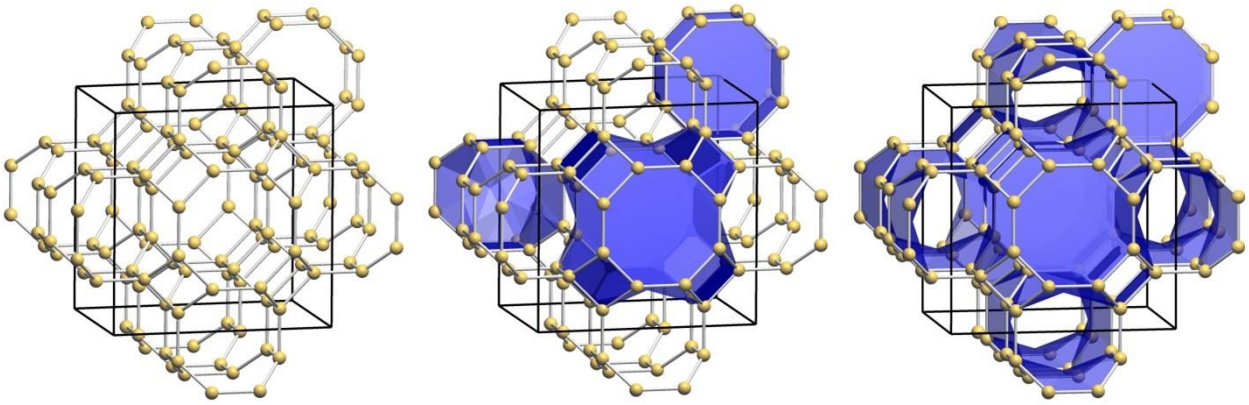

Fig. 1 Zeolite merlinoite (MER) crystal structure: (left) a fragment of periodic net with the unit cell; (middle) three independent natural tiles with face symbols [4^2, 8^4] (left tile), [4^{12}, 8^6] (central tile) and [4^8, 8^2] (top right tile); the tiles are confined by three kinds of 4–membered (4*a*, 4*b*, 4*c*) rings and three kinds of 8–membered (8*a*, 8*b*, 8*c*) rings of the net; (right) the triply periodic surface generated by removing two kinds of 4–membered rings (4*a* and 4*b*) and one kind of 8–membered ring (8*b*) and represented by the 4*c*–,8*a*– and 8*c*–facets.

The resulting TPS divides the space into two non-intersecting parts (labyrinth), and if they are isomorphic to each other the TPS is considered to be balanced [30]. Geometrically, the obtained TPS has a faceted structure and requires smoothing to obtain the minimum mean curvature. Since the

number of periodic nets is infinite and more than 800,000 of them are stored in the TopCryst database [26], this approach has been used as a template for generating porous structures and metamaterials. In addition, a database of computer models of some newly discovered TPS has been created [18]. In this study, we fabricated porous materials using information from this database (Fig. 2).

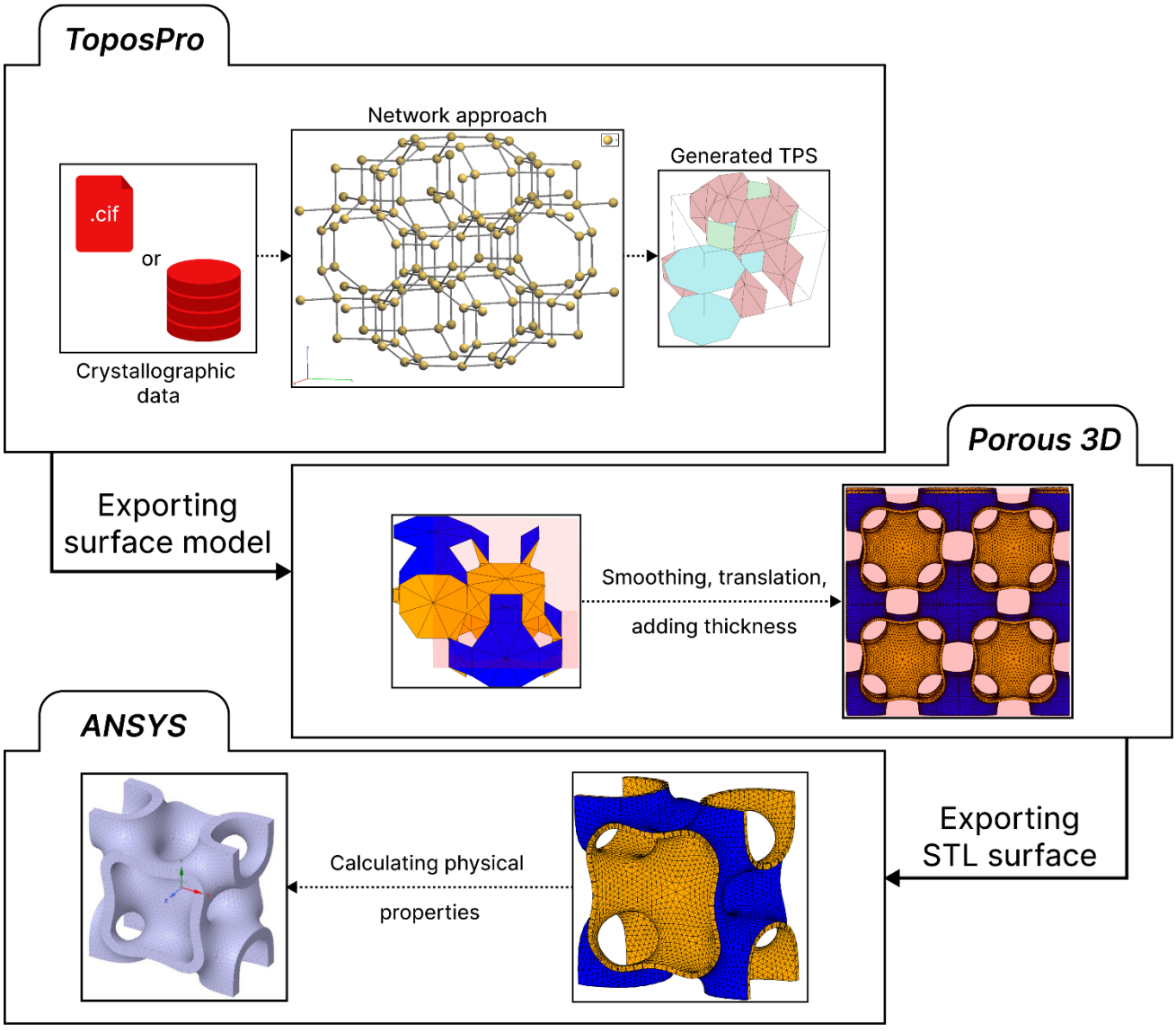

Fig. 2 Visual representation of the method used to generate porous material model from TPS based on the zeolite merlinoite (MER) structure using ToposPro, Porous 3D and to numerically study its mechanical and thermal properties with ANSYS software.

Let's discuss this procedure in more detail. The TPS facet model generated by ToposPro is output to a textual .t3g file, where the coordinates of all facets (rings) are given (Fig. 3):

– Obtained from periodic net tiling name (MER) and all of its independent (symmetry inequivalent) rings (4*c*, 8*a*, 8*c*), which were used to compose the tiling (Fig. 3, line 1).

– Unit cell parameters (Fig. 3, lines 2–3).

– Facet (tile) vertices data (coordinates in fractions of the unit cell dimensions) starting with keyword RING and its' face symbol (Fig. 3, lines 5–8). This data is present for all facets in the unit cell.

```
1  MER: 3D surface formed by rings: 4c, 8a, 8c
2  14.09200 (a)   14.09200 (b)   9.95400 (c)
3  90.00 (α)  90.00 (β)   120.00 (γ)
4  RING 4  c
5  0.61060   0.76710   0.65500
6  0.76710   0.61060   0.65500
7  0.76710   0.61060   0.34500
8  0.61060   0.76710   0.34500
9  ...
```

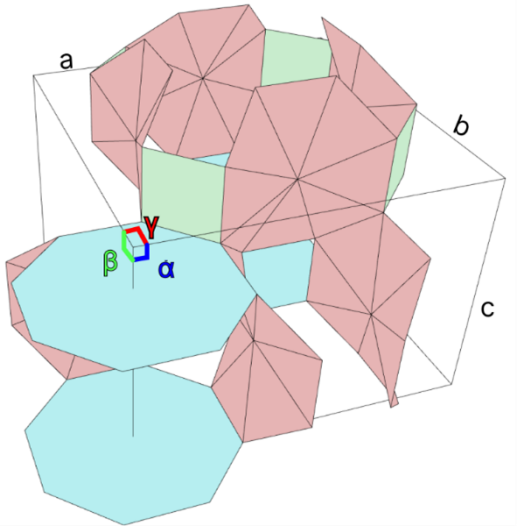

Fig. 3 The .t3g file generated by ToposPro for a TPS represented by eight (4*c*) 4– membered, eight (8*a*) and four (8*c*) different independent 8–membered rings of the periodic net obtained for the zeolite merlinoite (MER) crystal structure as well as dimensions and angular parameters of the unit cell.

Previously developed Porous 3D software [31] was used to visualize, translate, smooth and thicken the TPS model imported from ToposPro .t3g file. The resulting models can be exported to 3D printable STL–format file commonly supported by many computer–aided design and engineering software. We should note that STL format is used in our algorithms only in exporting the model to various CAD, CAE programs or for 3D printing and we do not manipulate the geometry of the output STL file. The following algorithms are implemented in this software:

– *Model translation algorithm* (Fig. 4). The unit cell of the imported TPS frame is a translationally in-dependent part of an infinite TPS. Obtaining larger parts of an infinite TPS implies parallel translation in space in rectangular coordinate system (*x*, *y*, *z*) of copies of a unit cell and "gluing" their boundaries. The following method is implemented analytically. Let *M* be the model that needs

to be translated and $v^i \in M$ is a vertex of this model with (v_x^i, v_y^i, v_z^i,) coordinates. To translate *M*, we need to calculate the translation matrix *T* based on the unit cell parameters *a*, *b*, *c*, *α*, *β*, *γ*:

$$T = \begin{pmatrix} 1 & 0 & 0 & t_x \\ 0 & 1 & 0 & t_y \\ 0 & 0 & 1 & t_z \\ 0 & 0 & 0 & 1 \end{pmatrix}, \quad (1)$$

$$t_x = \begin{bmatrix} a \\ b\cos\gamma \\ c \end{bmatrix}, t_y = \begin{bmatrix} a\cos\beta \\ b \\ c\cos\alpha \end{bmatrix}, t_z = \begin{bmatrix} a\cos\alpha \\ b\cos\beta\cos\gamma \\ c \end{bmatrix}.$$

So, using calculated matrix we can translate copied M vertices in any direction along t_x, t_y, t_z like this:

$$TM(i) = \begin{pmatrix} 1 & 0 & 0 & n_x t_x \\ 0 & 1 & 0 & n_y t_y \\ 0 & 0 & 1 & n_z t_z \\ 0 & 0 & 0 & 1 \end{pmatrix} \begin{pmatrix} v_x^i \\ v_y^i \\ v_z^i \\ 1 \end{pmatrix} = \begin{pmatrix} v_x^i + n_x t_x \\ v_y^i + n_y t_y \\ v_z^i + n_z t_z \\ 1 \end{pmatrix}, \quad (2)$$

$$M_{copied} = \begin{bmatrix} v_x^i + n_x t_x \\ v_y^i + n_y t_y \\ v_z^i + n_z t_z \end{bmatrix},$$

where n_x, n_y, n_z is the number of models needed along translation vector (Fig. 4).

– The *algorithm for facet smoothing* (Fig. 4) utilizes both Laplacian–based and optimization– based methods to minimize the absolute difference between the maximum and minimum values of mean curvatures calculated at each vertex of the surface mesh [18]. The mean curvature is calculated with the Delaunay triangulation and theory of normal cycles of differential geometry [32]. We have not used the Laplacian, Taubin or others smoothing algorithms in their pure form because these algorithms do not account for the mean curvature of the surface. The smoothing algorithm should be applied to the surface mesh, which has no volume, thus there is no need to preserve the volume of the object as the mentioned algorithms require. We have checked our algorithm on the surfaces reported in Ref. [18] and found effect accuracy with the average deviation of the calculated mean curvature of 0.01%.

– *Assigning surface thickness* is carried out by moving copied points of the surface along their normal vector to the specified distance and restoring surface faces on the moved points. Then, additional polygons are created to fill the gap between the original surface and the copy, resulting in a contiguous volume (Fig. 5). We limit the thickness value of the model to avoid self–intersections in the case of too drastic change of the surface curvature. We plan to improve the algorithm and to remove this limitation in the next version of the Porous 3D software.

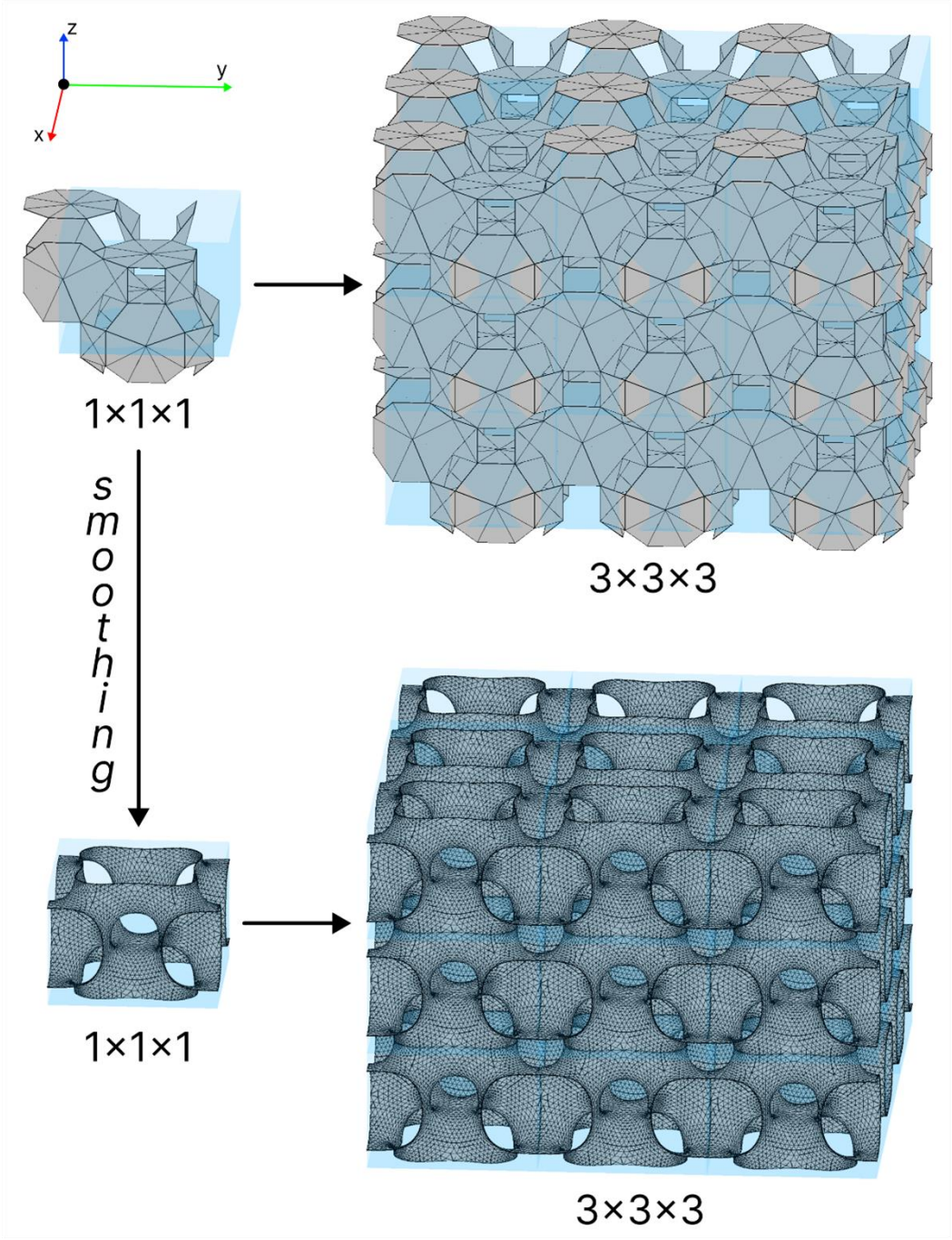

Fig. 4 Translating and gluing 27 unit cells of a TPS model generated from the zeolite merlinoite (MER) net. The boundaries of the internal unit cells (highlighted in light blue on the left) were removed after translating.

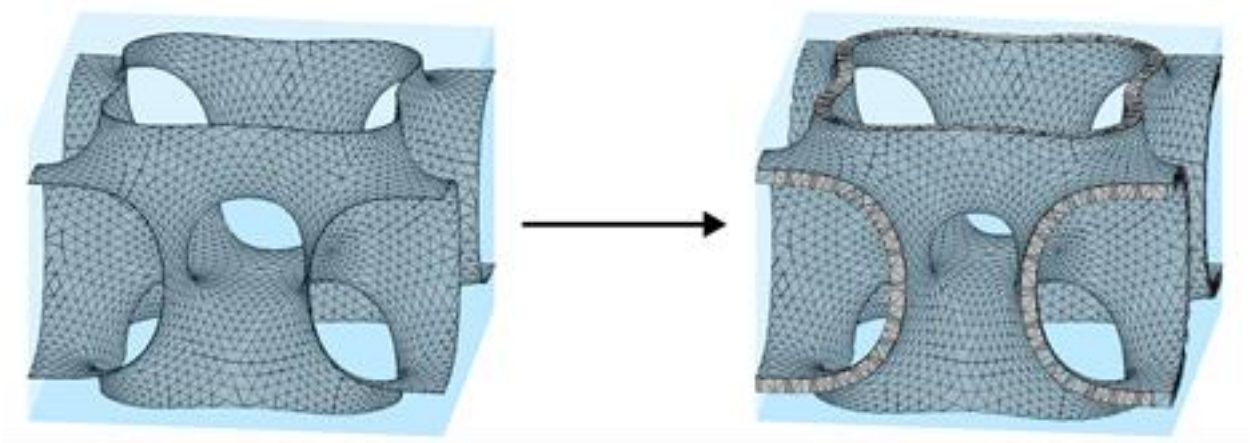

Fig. 5 Assigning thickness to a smoothed TPS model generated from the zeolite merlinoite (MER) net.

The surfaces constructed in this work by the described method are shown in Table 1 and Fig. 6 The thermal and mechanical properties of these surfaces are studied below. In Ref. [19] we investigated the mechanical properties of structures based on only minimal surfaces generated from zeolites by our method. In the present work the choice of zeolites for constructing surfaces was carried out in terms of establishing correlations between physical properties and surface symmetry properties. Therefore, we chose two zeolites with a high cubic symmetry of atomic networks (space group No. 229), one zeolite with a network close to them (space group No. 221), four zeolites with a lower tetragonal symmetry (space group No. 139) and one zeolite with sufficiently low rhombic symmetry (space group No.61). Using the ToposPro software package, the topological structures of the resulting surfaces were established.

Table 1 Topological and geometrical features of TPSs used in this work (Fig. 6).

Surface (zeolite)	TPMS analog	Space group	Genus	Labyrinth nets topology	Hopf ring net (HRN) topology	Balanced property	Tiling rings types
SOD	P	Im-3m	3	pcu; pcu	(nbo)	True	6*a*
RHO	C(P)	Im-3m	9	ftw;ftw	(14^2, 16, 22, 28^3, 32^2, 36, 44, 46, 50, 52, 56, 58, 60^3, 62, 66, 68–*c*)	True	4*b*, 6*a*, 8*a*
LTA	P	Pm-3m	3	pcu; pcu	(nbo)	True	4*b*, 6*b*
BCT	P	I4/mmm	3	pcu; pcu	(nbo)	True	8*c*
SAS	P	I4/mmm	3	pcu; pcu	(nbo)	True	4*a*, 4*b*, 6*a*
MER	I-WP	I4/mmm	4	nbo;bcu	(4, 6^3, 8^2, 12, 14–*c*)	False	4*c*, 8*a*, 8*c*
ATN	P	I4/mmm	3	pcu; pcu	(nbo)	True	4*a*, 8*b*
JSW	P	Pbca	3	pcu; pcu	(nbo)	True	4*a*, 4*b*, 4*c*, 6*c*, 6*d*

As can be seen from Table 1, surfaces belong into three well known types: P–surfaces, complementary to P–surfaces (C(P) or Neovius surface) and I–WP surface [18,33]. All obtained surfaces have a system of two non–intersecting labyrinths with different properties of balance.

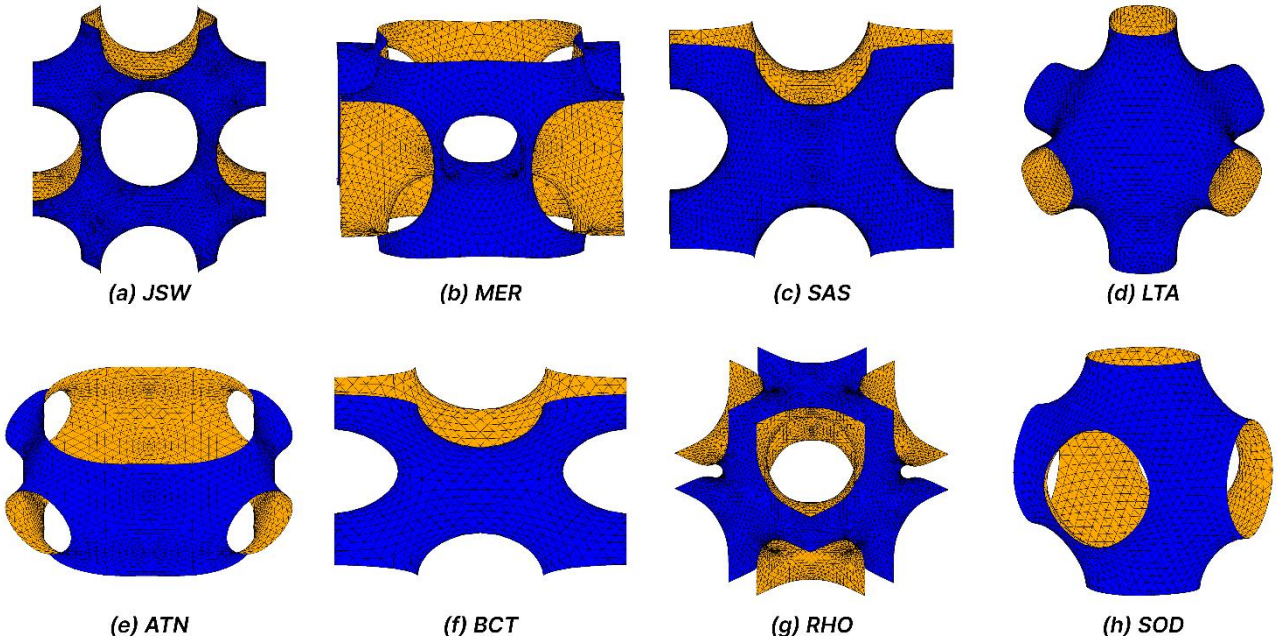

Fig. 6 Unit cells of TPSs present in this work. a) TPS (P surface) based on CoAPO–CJ62 (JSW) zeolite; b) TPS (I-WP surface) based on Merlinoite (MER) zeolite; c) TPS (P surface) based on STA–6 (SAS) zeolite; d) TPS (P surface) based on Linde Type A (LTA); e) TPS (P surface) based on MAPO–39 (ATN) zeolite; f) TPS (P surface) based on Mg–BCCT (BCT) zeolite; g) TPS (C(P) Neovius) based on Rho (RHO) zeolite; h) TPS (P surface) based on Sodalite (SOD) zeolite.

Now let's discuss the relationship of surfaces from Table 1 with surfaces from the minimal surfaces database [34] which implements the methods from Ref. [33] Only the SOD surface from Table 1 is fully equivalent to the corresponding surface from Ref. [34] The rest of the surfaces, although having the same topology as the corresponding surfaces from Ref. [34] differ from them geometrically and are new. We note once again that the surfaces obtained in this work are closest to the minimum ones, since in our facet smoothing algorithm (see Fig. 5), the condition of the minimum modulus of mean curvature is implemented. Using SpaceClaim module of ANSYS [21] porous structure is converted to solid–state geometry (Parasolid) format to numerically investigate its physical properties.

All calculated topological and geometrical features of 98 TPSs described in Ref. [18] (Supplementary Information) were used to determine which known TPMSs can be generated with the

zeolite dataset. Let us briefly recall the definitions of the topological features used. Labyrinth nets topology is the topology of the graph representing two independent pore systems of a generated TPS. Hopf ring net (HRN) topology is the topology of the graph whose vertices coincide with the barycenters of the TPS rings and the barycenters of catenated rings, which are built on geometrical centers of the rings of the labyrinth net. HRN is used to determine the method of interweaving of the labyrinth nets. TPS is balanced if it divides the space into two congruent labyrinths. All features described above are crucial for determining known TPMS analogs of our surfaces, i.e. P, C(P), I–WP, F–RD, G, H and other TPMSs.

Below we consider how this method is applied to the investigation of thermophysical and mechanical properties of the TPS from the Table 1. Note that other recent studies [5,6,8–12,35–37] where the porous structures were modeled from TPS applied an analytical formulae for constructing these known TPS. All of the surfaces generated by our method (see Table 1) cannot be created by existing methods especially new minimal surfaces. The described method constructs TPS based on crystal structure so surfaces are unique in their geometry even if they are similar in their topological properties to existing ones, and are not described by any analytical expressions.

The presented method does not require any analytical representations to generate TPSs and new TPSs obtained by our approach also don’t have any exact formulae yet. Therefore, the theoretical part of our study included the following stages:

1. TPS frame is generated from the periodic net obtained from crystal structure data us-ing ToposPro and then is exported into a .t3g file.
2. Imported in Porous 3D TPS is then processed by developed algorithms and saved as .stl model file.
3. Using ANSYS we numerically investigate thermophysical and mechanical properties of obtained .stl model as described below.

3 Experimental and numerical study of thermophysical properties of the obtained porous structures

In this paper we investigate effective conductivities of porous structures with novel triply periodic solid shell architecture. Despite the ordered macrostructure, the thermal properties of porous materials cannot be considered isotropic. Thermal conductivity values that characterize heat transfer are different at different points of medium and depend on heat transfer direction.

Thermophysical properties for isotropic bodies can be identified by solving the inverse thermal conductivity problem. However, the problem becomes much more complicated for anisotropic materials, which is the case of our study since the periodic TPS structure intends a high degree of anisotropy of the sample.

Fourier's law is formulated in an anisotropic media as

$$\mathbf{q} = -\mathbf{k}\nabla u, \tag{3}$$

where $\mathbf{q}$ is heat flux vector, $\mathbf{k} = [k_{ij}](i,j = \overline{1,3})$ is symmetric thermal conductivity second-rank tensor and ∇u is temperature gradient.

With Eq. (3) energy conservation equation (heat equation) can be written as follows

$$\rho c_p \frac{\partial u}{\partial t} = -div(-\mathbf{k}\nabla u) + q_V, \tag{4}$$

where c_p is specific heat capacity, ρ is material density, t is time and q_V is internal heat energy per unit volume at each point and time.

Since thermal conductivity $-\mathbf{k}$ is tensor, the heat fluxes at each point of the area under study are different in different directions. It follows from Eq. (4) that to account for the properties anisotropy one needs to solve multidimensional equations containing mixed differential operators. Additional difficulties arise when setting the boundary conditions for Eq. (4) since the heat fluxes need to be determined taking into account the boundary behavior, i.e., direction cosines to the boundary with respect to the selected coordinate system [38].

The difficulties mentioned above significantly limit the possibilities of applying classical analytical methods for the theoretical evaluation of the thermal conductivity tensor elements $[k_{ij}](i,j = \overline{1,3})$. In this regard, various methods of medium homogenization are used to describe the temperature state of anisotropic media: RVE, MsFEM, etc.

Thus, in Ref. [39] the representative volume element (RVE) method - is introduced into consideration, where RVE is the minimum volume of an anisotropic body that reproduces its thermal properties. In Ref. [40] M. I. Epov et al. use the multiscale finite element method (MsFEM), etc. In this paper, we use the RVE method of medium homogenization. Note that in our approach the computer representation of new porous structures enables one to easily implement any method of medium homogenization, including the RVE method although for most of our surfaces there is no representation in the form of an analytical expression.

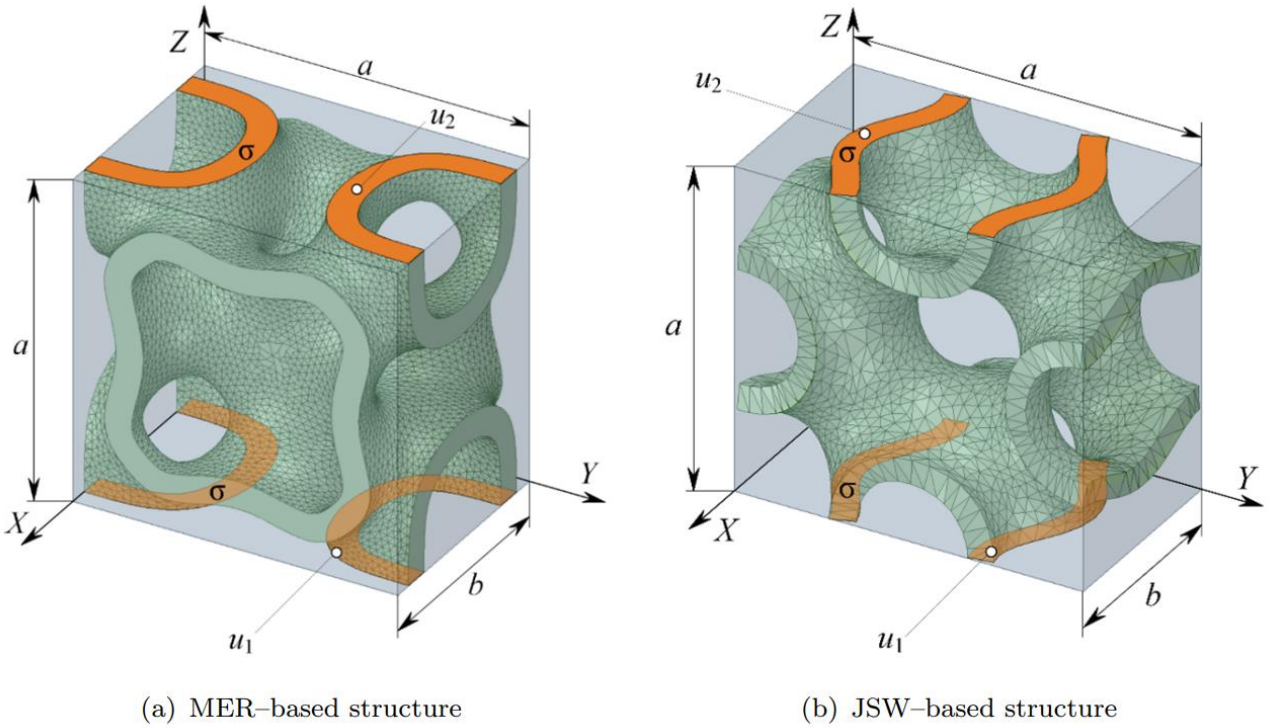

Fig. 7 RVE–scheme with the inscribed solid shell. a) is merlinoite (MER–based) structure, b) is CoAPO–CJ62 (JSW–based) structure. u_1, u_2 are the boundary temperatures; σ is the area of the unit cell in cross section.

In order to determine the integral thermal characteristics of a unit cell element, for example, of the MER–based TPS (Fig. 7) along z axis, we assume that thermophysical properties at any point in the

unit cell volume are isotropic. That is, we consider the volume under study to be filled with a homogeneous medium with constant effective thermal conductivity and effective coefficient of thermal conductivity k_{eff}. The anisotropy of properties caused by the features of 3D printing using the FDM method has a great influence on the results of experimental studies. In particular, when studying the thermal conductivity of samples in which the rasters are laid along and perpendicular to the direction of the heat flow, differences in measurements can reach 50%. It is worth noting that the smallest deviation from the thermal conductivity of the original material is observed when rasters lie in the direction of the heat flow. Studies [41,42] show that with optimal raster direction and 100% fill ratio, the discrepancy between the thermal conductivities of the original material and the sample does not exceed 5–10%. In this work, for an experimental study of thermal conductivity, samples were made in which rasters direction coincides with the direction of the heat flow at 100% fill ratio. In this way, the error caused by anisotropy is minimized and is acceptable for research purposes.

If the heat transfer occurs only along z axis, the heat flow Q across any orthogonal section of the unit cell is determined as follows:

$$Q = \overline{q_S} S, \tag{5}$$

where

$$\overline{q_S} = \frac{1}{S}\int_{\sigma} q d\sigma, \tag{6}$$

$\overline{q_S}$ is average density of heat flux in the cross-section $S = ab$, q is actual density of heat flux in the cross-section $\sigma = S(1 - s)$, $s = S_l/S$ is specific pore area and S_l is pore area in the cross-section under consideration.

On the other hand, according to Fourier's law

$$\overline{q_S} = -k_{eff}\frac{\partial u}{\partial z}, \tag{7}$$

It follows from Eq. (4) that for the stationary mode of heat transfer, the temperature distribution in the homogenized medium along z coordinate changes according to a linear law. Then the following relation is valid

$$\overline{q_S} = -k_{eff}\frac{u_2-u_1}{a}, \quad (8)$$

where u_1, u_2 temperatures at the cell boundaries.

Given that $S = ab$ we have from Eq. (6) and (8)

$$k_{eff} = \frac{\overline{q_S}a}{u_2-u_1} = \frac{\int_\sigma q d\sigma}{b(u_2-u_1)} \quad (9)$$

To determine the actual value of the heat flux in the cross section that is perpendicular to z axis, we use the specific surface of the pores *s*. Analysis of the dependence $s(Z, \Delta)$ (Fig. 8) shows that the pore is symmetrical with respect to $Z = 0.5$ with the equality of s values at $Z \in [0; 0.5; 1]$. This can be explained by the fact that the creation of pores in the principal direction leads to the formation of two independent pore systems. Obviously, the average density of the heat flux $\overline{q_\sigma}$

$$\overline{q_\sigma} = \frac{\overline{q_S}}{1-s}, \quad (10)$$

which can be determined from the ANSYS numerical modeling as the average heat flux, is greater than the corresponding $\overline{q_S}$ value at any point of the *S* cross-section.

Given Eq. (10), equivalent thermal conductivity is determined as follows:

$$k_{eff} = \frac{a\overline{q_\sigma}(1-s)}{u_2-u_1}, \quad (11)$$

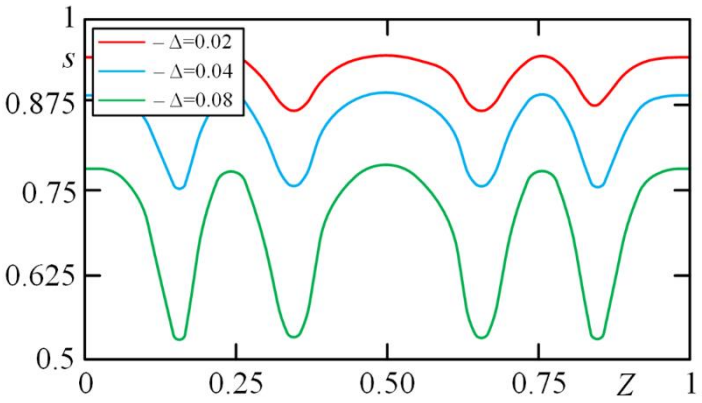

Fig. 8 Dependence of *s* on $Z = z/a$ for different values of specific wall thickness $\Delta = \sigma/a$ along *z* axis.

The unit cell shown in Fig. 7 is an RVE–element. Therefore, the determination of its thermal characteristics allows one to describe the temperature state of the media consisting of many unit cells subject to perfect thermal contact. Obviously, we can obtain structures with specified thermal

characteristics by combining the unit cells as well as by changing the wall thickness of the solid shell and the cell sizes.

We applied the following conditions for the CAE modeling of heat transfer in ANSYS:

(i) heat transfer mode is stationary;

(ii) heat transfer occurs along one of the axes of the orthogonal coordinate system (specifically z axis);

(iii) the first-kind boundary conditions, temperatures $u_1 = 0$ °C, $u_2 = 100$ °C, are set on the upper and lower faces of the solid shell, respectively (Fig. 7);

(iv) adiabatic wall condition is set on the entire surface of solid shell except the top and bottom faces;

(v) the thermophysical properties of solid shell are known (Table 2).

Table 2 Thermophysical properties of the SBS filament.

Material characteristics	Value	Unit
Type of material	SBS	
Conductivity coefficient	0.2	$W \cdot m^{-1} \cdot {}^{\circ}C$
Heat capacity	1,000	$J \cdot kg^{-1} \cdot {}^{\circ}C$
Density	1,010	$kg \cdot m^{-3}$

Based on condition (ii), it follows that the heat transfer along *x* and *y* axes can be ignored. According to condition (iv) we neglect convective heat transfer. This assumption does not significantly affect the accuracy of modeling for natural convection in the pore space (at $a < 5$ mm).

The calculation results for the scalar temperature field (Fig. 9) and the vector field of heat flux (Table 3) enabled us to study the behavior of k_{eff} when changing the unit cell size (a) and the wall thickness (σ) of the material.

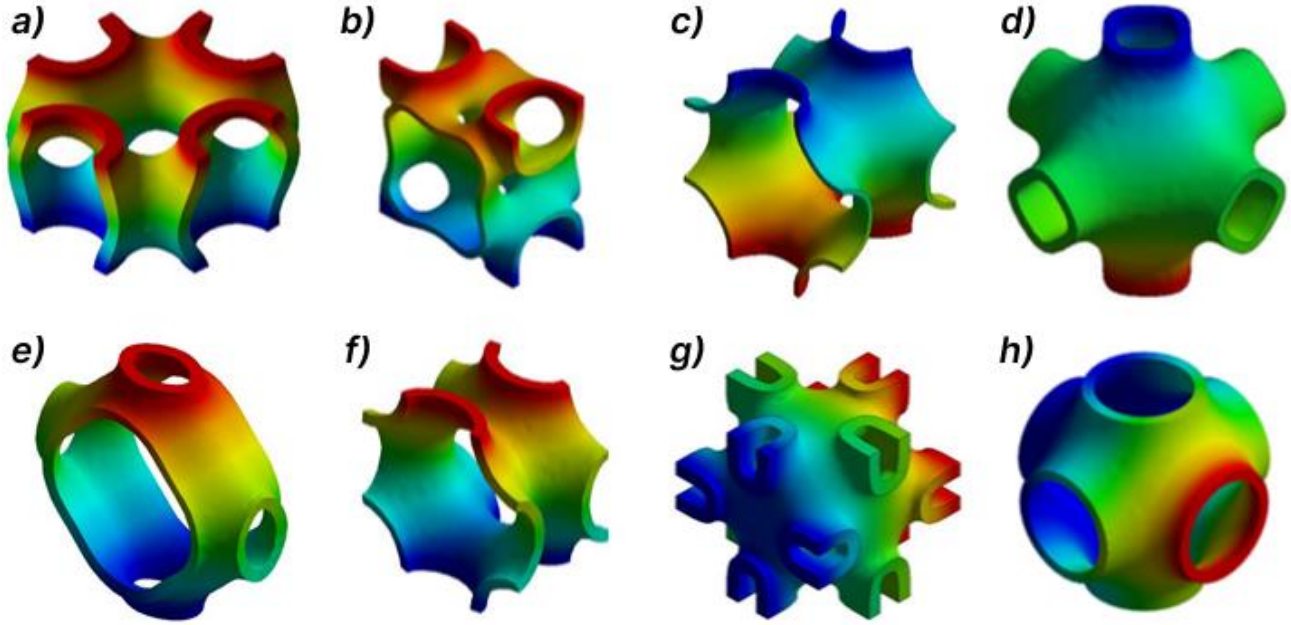

Fig. 9 Scalar temperature fields from 0 ˚C (navy blue) to 100 ˚C (red) for JSW–, MER–, SAS–, LTA–, ATN–, BCT–, RHO–, SOD–based structures a) –h), respectively.

Table 3 Average heat flux Eq. (10) for the scalar temperature fields.

$W \cdot m^{-1} \cdot ^{\circ}C$		
Structure	Along z axis	Along x axis
JSW	3,764	6,842
MER	3,497	4,873
SAS	2,843	4,025
LTA	3,893	3,893
ATN	3,421	9,217
BCT	3,873	6,177
RHO	3,836	3,836
SOD	3,674	3,674

The dependence $k_{eff}(\Delta)$ is linear (Fig. 10), while scaling the unit cell results in a proportional change of k_{eff}; for example, $k_{eff}(\Delta) = 2k_{eff}(2\Delta)$. The relationship between volume and surface area as the size of the TPMS increases or decreases has been described by the square-cube law.

Analysis of Fig. 10 shows that a required value keff can be obtained by changing the wall thickness σ or unit cell size a. For example, value k_{eff} = 0.0159 for MER–based material along *z* axis can be obtained at relative pore wall thickness Δ = 0.03, which can be defined as $\frac{\sigma}{a} = \frac{0.15}{5} = \frac{0.3}{10}$ etc. Therefore, a material with calculated thermophysical properties can be created by changing structural macroparameters of the unit cell.

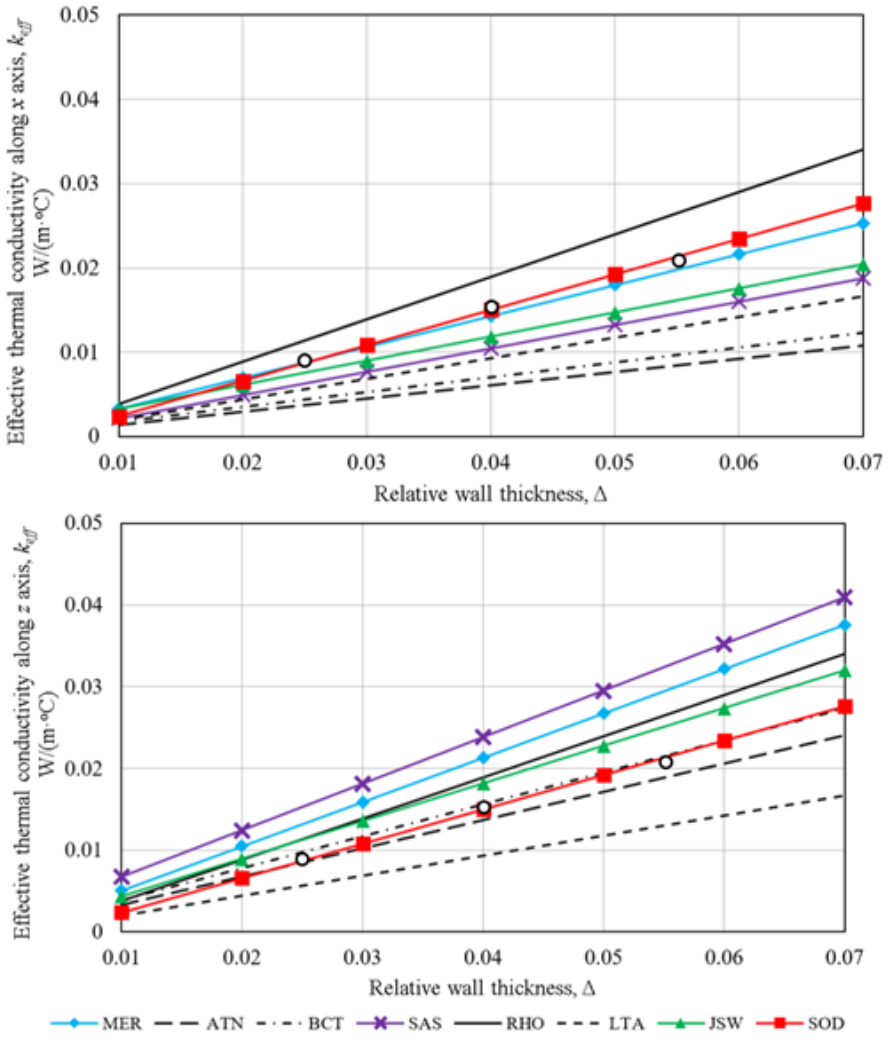

Fig. 10 Dependences of the effective thermal conductivity on relative wall thickness for surfaces from Table 1; white circles are experimentally obtained data on the effective thermal conductivity of a SOD–based structures.

When choosing the configuration of a porous structure, it is necessary to specify strength indicators. Thus, shrinking the unit cells leads to hardening the structure. On the other hand, enlarging the unit cell results in increasing the influence of the convective component.

In order to verify the adequacy of the modeling results, an experimental verification was performed. Using additive printing technology, the panel of a porous material with a size of 200×200×20 mm was made by the TOTAL Z Anyform L250G3-2X printer by FDM method (Fig. 11). When printing, the SBS filament with the properties specified in Table 2 was used. The printing was done with recommended settings: layer height – 0.15 mm; print speed – 15 mm·s^{-1}; nozzle temperature – 220 ˚C.

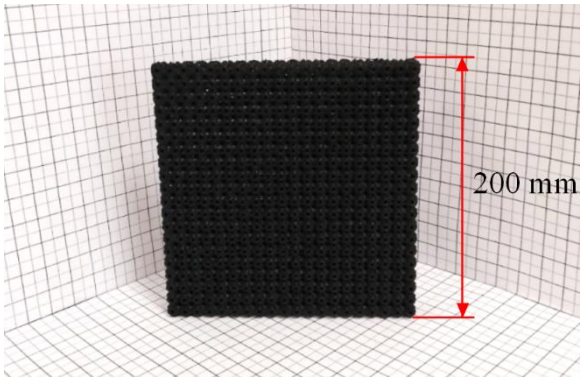

Fig. 11 A sample made of the SOD–based porous structure manufactured from SBS by FDM method.

Determination of thermal conductivity coefficients k_{eff} was carried out on a certified experimental setup ITP-MG4, which included a fridge and a heater to keep constant temperatures u_1, u_2 on the surfaces of the test sample. Thermal conductivity coefficient k_{eff} was determined according to relation Eq. (7) with an error of no more than 5%. By approximating theoretical and experimental data we obtained a relation for determining the value of the effective thermal conductivity coefficient at different Δ:

$$k_{eff}(\Delta) = C_1\Delta + C_2, \quad (12)$$

where C_1 and C_2 are the fitting constants for the function, which are presented in Table 4.

Table 4 The fitting constants of thermal conductivity coefficients $\boldsymbol{k_{eff}}$ Eq. (12) for two different directions. The fitting constants are measured in $W{\cdot}m^{-1}{\cdot}{}^{\circ}C$.

	Along *z* axis		Along *x* axis	
Structure	C_1	C_2	C_1	C_2
JSW	0.286	3.593E-04	0.460	-2.695E-04
MER	0.366	-3.593E-04	0.542	-3.593E-04
SAS	0.277	-5.988E-04	0.569	1.018E-03
LTA	0.245	-4.790E-04	0.245	-4.790E-04
ATN	0.157	-2.096E-04	0.345	-1.198E-04
BCT	0.176	-2.994E-05	0.390	2.096E-05
RHO	0.503	-1.198E-03	0.503	-1.198E-03
SOD	0.420	-1.800E-03	0.420	-1.800E-03

To determine heat capacity and density, we used the porosity ratio, which $\phi = V_P/V$ is equal to the ratio of the pore volume V_P to the volume of the entire unit cell. For the TPS-based materials the porosity $\phi = V_P/V$, where V_P is the pore volume, is a linear function of the relative wall thickness:

$$\phi = A_1\Delta + A_2, \quad (13)$$

where A_1 and A_2 are the fitting constants for the function.

Given Eq. (13), volume heat capacity and density are determined by relations:

$$\boldsymbol{c} = \boldsymbol{c_m}(\mathbf{1} - \boldsymbol{\phi}), \quad (14)$$

$$\boldsymbol{\rho} = \boldsymbol{\rho_m}(\mathbf{1} - \boldsymbol{\phi}), \quad (15)$$

where $\boldsymbol{c_m}$, $\boldsymbol{\rho_m}$ are heat capacity and density of the material, respectively.

Thus, the paper presents the results of comprehensive studies of porous structures based on TPS. The results obtained for SBS can be extended to other structures and other forms of the unit cell. Relations Eq. (12) – (15) enable one to determine the properties of the designed structure with high accuracy without performing additional calculations.

4 Experimental and numerical study of main mechanical properties of the obtained porous structures

Investigation of the mechanical properties of the atomic RVEs structures described in Sec. 2 porous samples were manufactured by additive technology from photopolymer resin "Phrozen Aqua-Gray-Resin" (polyamide PA-12) (Fig.11) with the properties given in Table 5. The samples are single RVEs for MER–based and JSW–based structures (see Fig. 12) sewed in three orthogonal directions in the amounts of 2×2×2, 3×3×3, and 4×4×4. Single RVEs have L×W×H of 10.63×8.83×10.63 mm and 8.14×8.14×4.91 mm for MER–based and JSW–based structures, respectively. The wall thickness in the samples is 0.2 mm.

Using Phrozen Sonic Mighty 4K LCD photopolymer printer we produced several samples by method of layer-by-layer solidification under UV according to recommended settings: layer maximum height – 0.05 mm; number of acceptable substrate words – 6, substrate illumination time – 50 s;

remaining layers illumination time – 5 s; maximum lifting height – 8 mm; lifting and retraction speed – 60 mm·min^{-1} and 150 mm·min^{-1}, respectively.

Table 5 Properties of the PA-12 material.

Property	Value	Unit
Density	1.27	*g·cc^{-1}*
Viscosity	1.5	*poise*
Tensile elongation	7	*%*
Tensile strength	0.02	*GPa*
Hardness	623	*Vickers*
Tensile modulus	0.192	*GPa*
Notched Izod impact strength	6,780	*J·m^{-2}*

Mechanical properties of specimens manufactured from PA-12 significantly depend on the 3D printing mode. Before studying porous samples, experimentally measurement of the mechanical characteristics of PA-12 after 3D printing procedure is necessity. For this purpose, several solid rectangular parallelepipeds the sizes of which are indicated above were manufactured using the same technology and equipment.

Following other recent studies porous structure [7–14] we have carried out the compression tests on our samples in order to experimentally measure their mechanical moduli. Tensile testing machine SHIMADZU was used for measurement of the compression characteristics of all samples in the automatic mode. Rate of compression was 1 mm/min. All measurements errors were less than 0.01%.

Stress-strain curve obtained experimentally was averaged for all similar solid samples. Linear incensement of strain revealed at low deformation stress and plastic strain area on the graph up to the stress of 49.33 MPa. For such materials this behavior is typical [43].

Using experimental data, the average value of the elastic compression modulus was E_c = 1.07 ± 0.04 GPa in the range ε = 1–3% and the Poisson ratio as approximate equal 0.4. This value falls within the acceptable range of this characteristic for a polyamide polymer at standard room temperature [43].

JSW–based and MER–based samples (Fig. 12, a) and b), respectively) were investigated using a similar experimental technique as for continuous samples. The experimental loading curves are shown in Fig. 13. The position of the curves depends on the number of RVEs in the sample, and curves with different numbers of RVEs are similar. The difference in the shape of the curves for the MER-based and JSW–based samples is due to the difference in the topological and geometric features of corresponding surfaces, given in Table 1. It can be seen from the Fig. 13 that the MER–based sample is characterized by the presence of an elastic deformation region and a slow growth to a maximum before failure. The JSW–based curve contains a pronounced maximum after the elastic section and subsequent oscillations before destruction. Both of these types of curve behavior take place for known porous materials obtained on the basis of triply periodic surfaces different from ours [1,11].

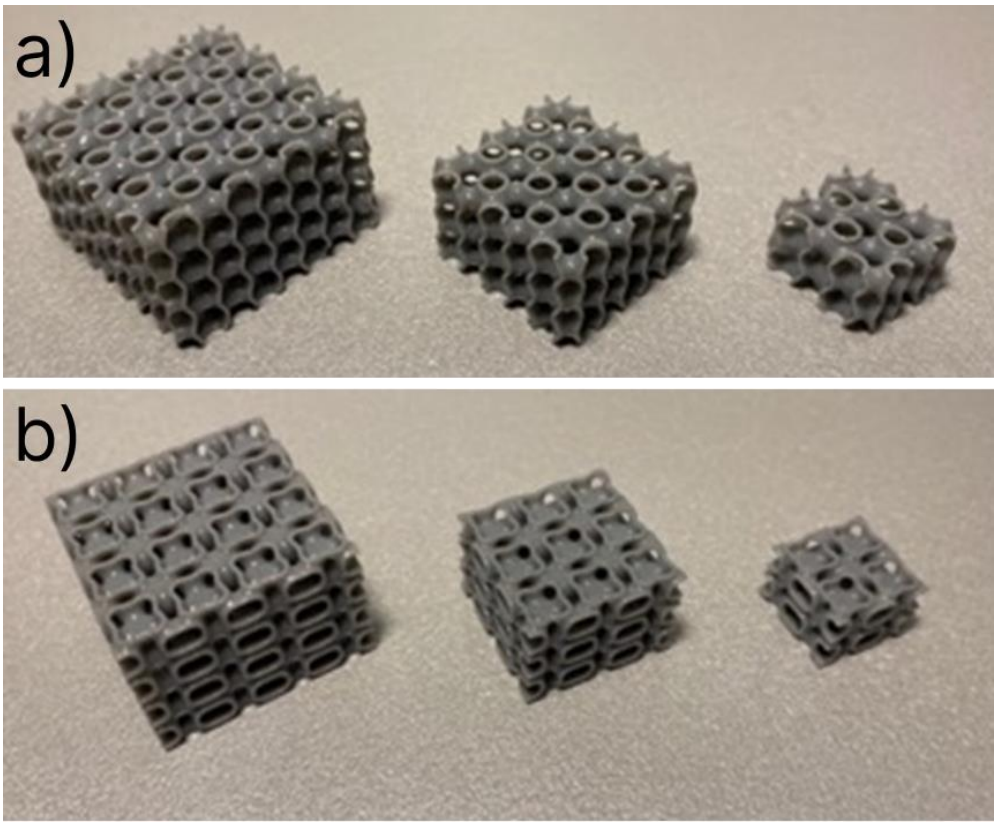

Fig. 12 Samples made of the a) JSW–based and b) MER–based porous structures manufactured from PA-12.

The experimental compression moduli E_c were obtained by the slope's averaging of the curves within strain of 1–2% (Fig. 13). These experimental values are shown in Table 6 together with the results of the corresponding finite element (FE) calculations.

We note a fairly good agreement between the experimental and theoretical results for the compression moduli, which indicates the adequacy of the chosen theoretical model.

Table 6 The experimental and numerical elastic compression modules E_c for MER and JSW samples (Fig. 12). The compression module is measured in MPa.

	E_c, (MER)		E_c, (JSW)	
Samples	Experiment	FE calculation	Experiment	FE calculation
2×2×2	6.10 ± 0.21	6.03	7.63 ± 0.25	7.53
3×3×3	11.95 ± 0.42	12.03	8.43 ± 0.28	8.32
4×4×4	14.79 ± 0.49	14.86	11.76 ± 0.39	11.64

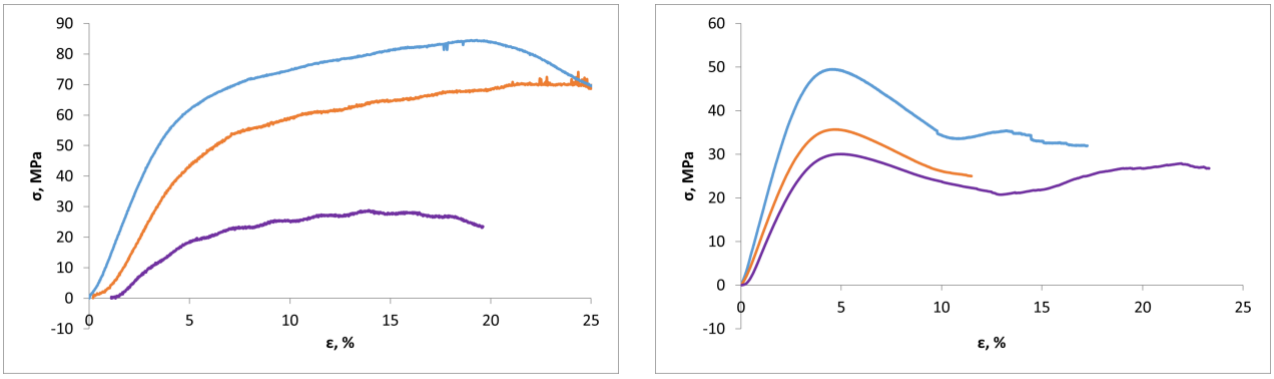

(a) MER–based structure (b) JSW–based structure

Fig. 13 Compressive stress–strain curves for a) MER–based and b) JSW-based samples with different numbers of RVE (see Fig. 12); upper curves (blue) are 4×4×4 samples, middle curves (orange) are 3×3×3 samples, lower curves (violet) are 2×2×2 samples.

The FE software ANSYS was used for the numerical modelling of compression test in order to find the elastic properties of porous samples MER–based and JSW–based samples, as well as for predicting mechanical properties of other porous materials (see Table 1) when changing their stress-strain state, and their geometrical parameters. Our simulation contains two main features. First, we considered polyamide as a material belonging to the class of hard rubbers, and only elastic deformations of this initial material were taken into account at modeling the mechanical properties of porous samples. Second, the patch control method was chosen as a method for generating a finite element grid using

tetrahedron elements with an average size close to 0.7 mm. But shell finite elements with a slightly smaller size were used to simulate RVE for 4×4×4 samples. A fairly good agreement between the results of theoretical calculations in the described model and experiment (see Table 6) makes it possible to model the mechanical properties of other porous materials based on TPS from Table 1 in the same way.

So, the distribution of von Mises mechanical stresses calculated by the FE method is shown in Fig. 14 for different single RVE. It can be seen from Fig. 14 that the stresses are distributed rather uniformly, that is apparently explained by the proximity of the surfaces constructed in this work to the minimum ones, as we discussed in Section 2 (see also Ref. [34]). Recall that our smoothing procedure from Section 2 includes the minimality mean surface curvature condition.

The components of the compression and shear modules, as well as the Poisson's ratios for a single RVE (Fig. 14) are presented in Table 7. For all single RVEs, the elastic compression modules E_{11}, E_{22}, E_{33} were calculated along main axes (Fig. 14). The Poisson coefficients v and shear modulus G for the unit RVEs were calculated using standard equations:

$$\mathrm{G_{ij}} = \frac{\tau_{\mathrm{ij}}}{\theta_{\mathrm{ij}}}, \nu_{\mathrm{ij}} = \frac{\varepsilon_{\mathrm{trans(i)}}}{\varepsilon_{\mathrm{axial(j)}}}, \quad (16)$$

where τ is tangential stress, θ is tangential relative deformation, $\varepsilon_{\mathrm{trans}}$ and $\varepsilon_{\mathrm{axial}}$ are transverse and longitudinal relative deformations, respectively.

However, it should be noted that all these calculations were made for the fixed thickness of the sample walls and the same initial material and are not have universal meaning. Nevertheless, the data in Table 7 can be used to evaluate the mechanical properties of porous materials relative to each other. For example, the isotropic RHO–based structure is the most stiffness in compression, the MER–based structure also exhibits greater stiffness in compression along one of the directions, the ATN–based structure is the most compliance in compression and the BCT–based structure has the highest shear resistance. Only LTA–based and RHO–based TPMS have identical mechanical parameters along principal axes, while remaining structures have substantially anisotropic behavior.

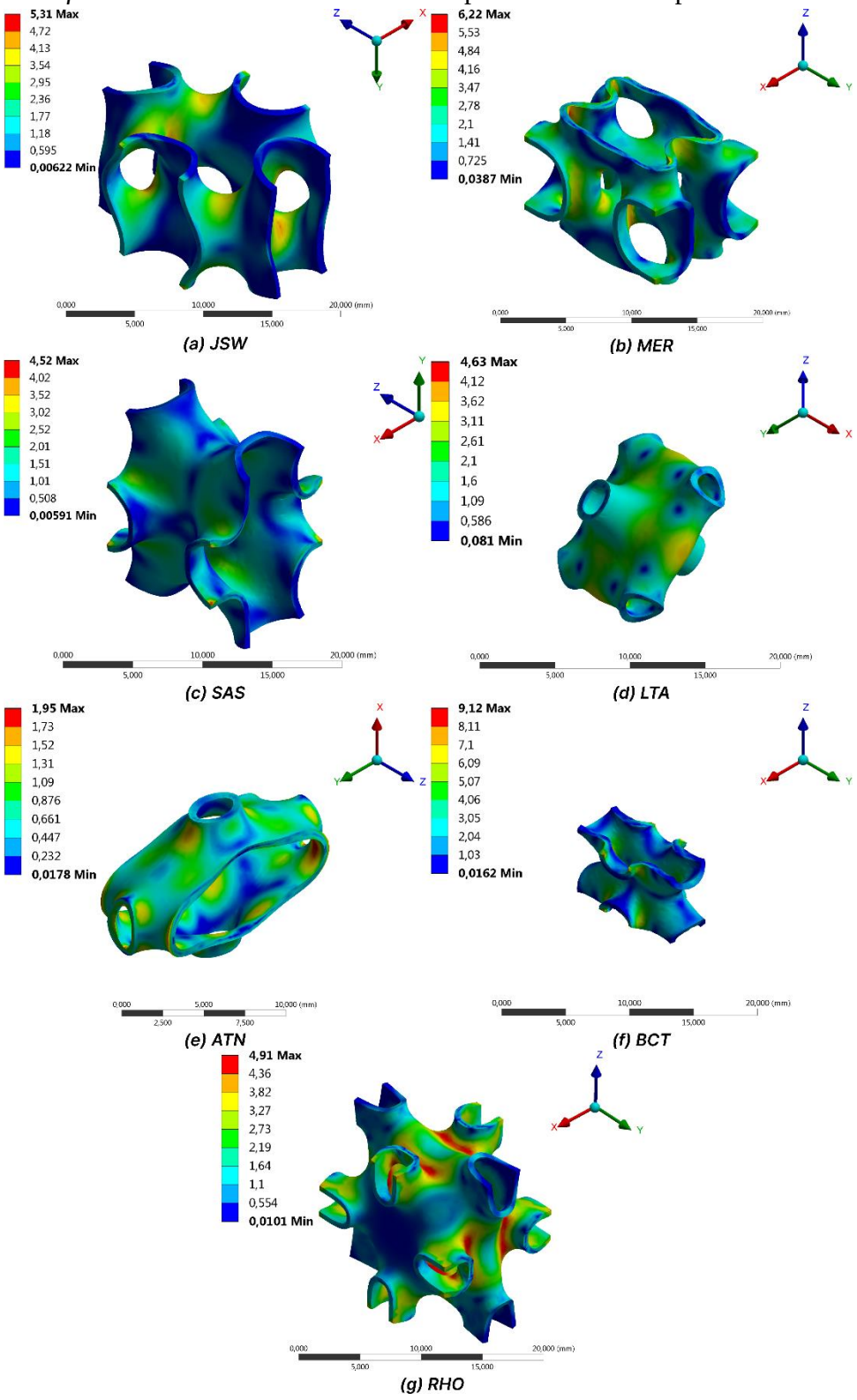

Fig. 14 Distribution of von Mises stresses in modeling compression in the ANSYS software by the finite element method for different single RVE with relative compressive deformation of 3%. JSW–, MER–, SAS–, LTA–, ATN–, BCT–, RHO–based structures are a) – g), respectively. Reds are the areas with the highest stress, blues are with the lowest ones.

Table 7 Mechanical characteristics of single RVE (see Fig. 14) obtained from the FE method. E_{11}, E_{22}, E_{33} – compression modules along the principal axes. The orientation in 3d space of the unit RVEs is shown in Fig. 14. Poisson's ratios v and shear moduli G defined by Eq. (16). The thickness of the wall is 0.2 mm. Units of modules is MPa.

Structure	E_{11}	E_{22}	E_{33}	G_{12}	G_{23}	G_{31}	υ_{12}	υ_{13}	υ_{23}
JSW	13.58	11.25	6.98	0.71	5.6	6.24	-0.10	0.79	0.73
MER	12.29	20.30	12.37	4.73	4.73	6.82	0.21	0.59	0.34
SAS	1.37	5.68	1.38	4.49	4.51	6.55	0.10	0.87	0.41
LTA	4.18	4.18	4.18	2.66	2.66	2.66	0.42	0.42	0.42
ATN	0.66	3.80	0.66	4.84	4.86	6.95	0.04	0.96	0.20
BCT	9.18	3.78	9.18	7.91	7.84	14.01	0.52	0.61	0.22
RHO	17.93	17.93	17.93	2.68	2.68	2.68	0.33	0.33	0.33

To obtain more universal estimates of the mechanical properties of the porous structures listed in Table 1, we used the well–known Gibson–Ashby relation [1]:

$$\frac{E^*}{E_{\mathrm{mat}}} = \left(\frac{\rho^*}{\rho_{\mathrm{mat}}}\right)^{\alpha}, \tag{17}$$

where, in one hand, E^* is the compression modulus ρ^* is the average density of the porous structure, and in another E_{mat} is the compression modulus ρ_{mat} is the density of the initial material; α is a topological–geometrical parameter, depending mainly on the properties of the TPMS.

As can be seen, the functional relation Eq. (17) does not depend on the type of the initial material, but is determined by the geometrical and topological characteristics of the porous structure. The main purpose of the Gibson–Ashby analysis in our work is to compare the mechanical properties of porous samples with different topological and geometrical structures. In this regard, we perform the appropriate calculations only for single RVEs with topological and geometrical parameters listed in Table 1. Modeling is carried out at small relative deformations during compression in the range of 1–3%.

The mechanical properties of the skeleton material were described only by its linear (elastic) moduli. Interesting problems of taking into account nonlinear effects, fatigue effects, as well as experimental verification of the results are beyond the scope of our paper. The results of the analysis of our calculations using the Gibson–Ashby relation Eq. (17) in the case of compression along the x and y axes are shown in Fig. 15. The mutual arrangement of the lines in Fig. 15 corresponds to the trend of

the values in Table. 7 and is similar to the results from article [11], in principle. Note that the close lines in Fig. 15 can describe the properties of porous structures, the characteristics for which from Table 1 can be very different. This means that a more detailed description of the topological and geometric properties of the surfaces is required in order to establish correlations between the topological-geometric properties of triply periodic surfaces and the mechanical properties of the corresponding porous materials. This will be done by us in the future. Nevertheless, the results shown in Fig. 15 can be used in engineering practice when choosing structural materials with optimal physical and mechanical properties, for example.

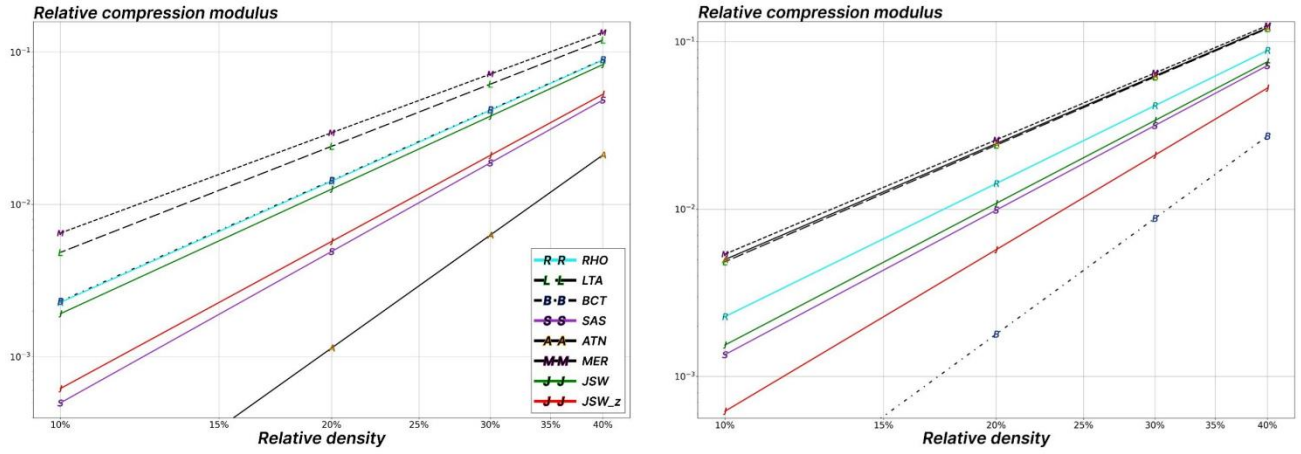

(a) x axis (b) y axis

Fig. 15 The results of the analysis of the mechanical properties of single RVE from Fig. 14 using the Gibson–Ashby relation (17) in the case of compression a) along the *x*–axis and b) along the *y*–axis; line with triangles down (red) is dependence for JSW–based structure at compression along *z*–axis.

An important feature of porous structures is the ability to absorb the strain energy [7–14]. We calculated the dependence of the strain energy density on the relative density for the porous structures constructed in our work (see Table 1). The calculations were carried out for the case of compression along the *x* and *y* axes. The results of the calculation are shown in Fig. 16. When comparing Fig. 15 and Fig. 16 it can be seen that the sequence of lines is the same. That is, the strain energy density absorbed by the porous structure corresponds to its stiffness. However, the relative distance between the lines in Fig. 15 and Fig. 16 can vary significantly. Thus, porous structures with almost the same

stiffness can absorb different amounts of strain energy. For example, this is clearly seen when comparing the upper groups of lines in Fig. 15 b) and Fig. 16 b).

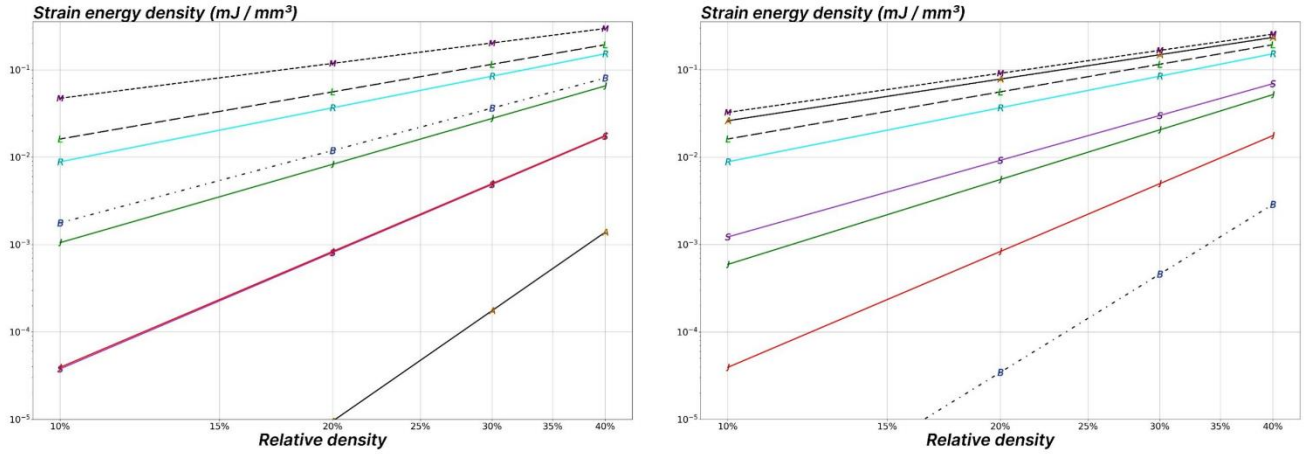

(a) x axis (b) y axis

Fig. 16 Dependence of the strain energy density on the relative density of the porous structure under compression along the *x* and *y* axes (a) and b), respectively); legend is the same as in Fig. 15a.

In total, Fig. 15 and 16 can be noted that the effect of the topology and geometry is more evident at smaller relative densities of porous materials and as the relative density increases, the all lines converges and the effect of the topology and geometry becomes less explicitly.

5 Conclusions

In this paper, porous structures are generated based on triply periodic surfaces (TPS) and their thermal and mechanical properties are studied. To generate porous structures, a method previously developed by the authors is used. Construction of porous structures in developed approach is carried out by three following procedures. First of them creates TPSs from a topological description of atom networks of the natural crystals by ToposPro software package. These TPSs are formed by polygons and divide the space in two disconnected parts. Other procedure performs smoothing TPS from the minimality condition of average curvature. Finally, after giving the surface some thickness, it is converted into a format used in 3D printing and in the most common application packages like ANSYS.

The developed approach makes it possible to generate, in fact, an unlimited number of new TPSs, on base of which new porous structures, composites, and metamaterials can be construct.

A database of constructed TPSs and corresponding tools have been built in the present paper. Investigation of thermal and mechanical properties of eight porous macroscopic structures generated from crystals of zeolites was conducted. These structures are varied by topological type, genus, spatial groups, topology of labyrinth nets, Hopf's nets topology, and balance properties. Samples of three of these structures were manufactured by 3D printing from SBS filament and polyamide PA-12 for experimental study and verification of numerical models.

We calculated scalar temperature fields, heat flux vector fields, as well as coefficients of effective thermal conductivity at different conditions for all obtained in our work samples. In particular, linear dependence of effective thermal conductivity coefficient on relative thick-ness walls of porous samples was identified. The thermal properties were modeled using the ANSYS software. Results of calculations are in good agreement with experiments.

Mechanical characteristics of porous samples were measured experimentally and elastic compression moduli and loading curves were obtained. Obtained dependencies are similar to ones for porous structures from other works. The numerical calculation of elastic compression moduli in the ANSYS software showed very good agreement with experiment. Numerical modeling of mechanical properties was performed for all porous structures obtained in our work. The components of the compression and shear modules, as well as the Poisson's ratios were calculated. The analysis of our results was carried out using the Gibson-Ashby relation and the dependence of the relative compression moduli on the relative density was obtained. In addition, the densities of strain energies were calculated as the functions of the porous structure's relative densities.

Thus, the results presented in the article indicate the effectivity of our method for constructing TPS and corresponding porous structures based on atomic networks of natural crystals, and also provide

the opportunity to select the most suitable structures for engineering applications from among ones considered in the article in terms of their thermal and mechanical properties.

References

[1] Gibson LJ, Ashby MF. *Cellular Solids: Structure and Properties*. Cambridge (UK): Cambridge University Press, 2014. https://doi.org/10.1017/CBO9781139878326

[2] Villani C. *Optimal transport: old and new*, Berlin (Germany): Springer Heidelberg, 2009. https://doi.org/10.1007/978-3-540-71050-9

[3] Ashby MF, Evans A, Fleck N, *et al*. *Metal Foams: a Design Guide*, Oxford (UK): Butterworth-Heinemann, 2000. https://doi.org/10.1016/B978-0-7506-7219-1.X5000-4

[4] Gunther F, Pilz, S, Hirsch F, *et al*. Shape optimization of additively manufactured lattices based on triply periodic minimal surfaces. *Additive Manufacturing* 2023, **73**: 103659. https://doi.org/10.1016/j.addma.2023.103659

[5] Li Z, Chen Z, Chen X, *et al*. Mechanical properties of triply periodic minimal surface (TPMS) scaffolds: considering the influence of spatial angle and surface curvature. *Biomechanics and Modeling in Mechanobiology* 2023, **22**: 541–560. https://doi.org/10.1007/s10237-022- 01661-7

[6] Yeranee K, Rao Y. A Review of Recent Investigations on Flow and Heat Transfer Enhancement in Cooling Channels Embedded with Triply Periodic Minimal Sur-faces (TPMS). *Energies* 2022, **15**: 8994. https://doi.org/10.3390/en15238994

[7] Lin ZH, Pan JH, Li HY. Mechanical Strength of Triply Periodic Minimal Surface Lattices Subjected to Three-Point Bending. *Polymers* 2022, **14**: 2885. https://doi.org/10.3390/polym14142885

[8] Maskery I, Aboulkhair NT, Aremu AO, *et al*. Compressive failure modes and energy absorption in additively manufactured double gyroid lattices. *Additive Manufacturing* 2017, **16**: 24–29. https://doi.org/10.1016/j.addma.2017.04.003

[9] Baghous N, Barsoum I, Al-Rub RKA. Generalized yield surface for sheet-based triply periodic minimal surface lattices. *International Journal of Mechanical Sciences* 2023, **252**: 108370 https://doi.org/10.1016/j.ijmecsci.2023.108370

[10] Wang YD, Lian YP, Wang ZD, *et al*. A novel triple periodic minimal surface-like plate lattice and its data-driven optimization method for superior mechanical properties. *Applied Mathematics and Mechanics (English Edition)* 2024, **45**: 217–238. https://doi.org/10.1007/s10483-024-3079-7

[11] Khedri E, Karimi HR, Aliha MRM, *et al*. Tensile, flexural, and mode-I cracking behavior of interpenetrating phase composites (IPC), developed using additively manufactured PLA-based structures with different infill densities and epoxy resin polymer as matrix. *Results in Engineering* 2024, **22**: 102162. https://doi.org/10.1016/j.rineng.2024.102162

[12] Wallat L, Selzer M, Wasmuth U, *et al*. Energy absorption capability of graded and non-graded sheet-based gyroid structures fabricated by microcast processing. *Journal of Materials Research and Technology* 2022, **21**: 1798–1810. https://doi.org/10.1016/j.jmrt.2022.09.093.

[13] Xia Q, Zhu J, Yu Q, *et al*. Triply periodic minimal surfaces based topology optimization for the hydrodynamic and convective heat transfer. *Communications in Nonlinear Science and Numerical Simulation* 2024, **131**: 107819. https://doi.org/10.1016/j.cnsns.2024.107819.

[14] Felix LC, Ambekar R, Tromer RM, *et al*. From pure mathematics to macroscale applications: the genesis of Schwarzites. *arXiv:2401.07884[cond-mat.mtrl-sci] 2024* :1–31. https://doi.org/10.48550/arXiv.2401.07884

[15] Perez J. New Golden Age of Minimal Surfaces. *Notices Of The American Mathematical Society* 2017, **64**: 347–358. http://dx.doi.org/10.1090/noti1500

[16] Cejka J, Morris RE, Nachtigall P. *Zeolites in Catalysis: Properties and Applications*. London (UK): The Royal Society of Chemistry, 2017. https://doi.org/10.1039/9781788010610

[17] Fischer M. Adsorption of Carbamazepine in All-Silica Zeolites Studied with Density Functional Theory Calculations. *ChemPhysChem* 2023, **24**: e202300022. https://doi.org/10.1002/cphc.202300022

[18] Smolkov MI, Blatova OA, Krutov AF, *et al*. Generating triply periodic surfaces from crystal structures: the tiling approach and its application to zeolites. *Acta Crystallographica Section A* 2022, **78**: 327–336. https://doi.org/10.1107/S2053273322004545.

[19] Eremin AV, Frolov MA, Krutov AF, *et al*. Mechanical properties of porous materials based on new triply periodic and minimal surfaces. *Mechanics of Advanced Materials and Structures* 2024, 1–17. https://doi.org/10.1080/15376494.2024.2303724

[20] Blatov VA, Shevchenko AP, Proserpio DM. Applied topological analysis of crystal structures with the program package ToposPro. *Crystal Growth & Design* 2014, **14**: 3576–3586. https://doi.org/10.1021/cg500498k.

[21] Thompson MK, Thompson JM. *ANSYS Mechanical APDL for Finite Element Analysis*, Oxford (UK): Butterworth-Heinemann, 2017.

[22] Baerlocher C, Mccusker LB, Olson DH. *Atlas of Zeolite Framework Types*, Amsterdam (Netherlands): Elsevier Science, 2007. https://doi.org/10.1016/B978-0-444-53064-6.X5186-X

[23] Arsentev MY, Sysoev EI, Makogon, AI, *et al*. High-throughput screening of 3D-printed architected materials in spired by crystal lattices: procedure, challenges, and mechanical properties. *ACS Omega* 2023, **8**: 24865–24874. https://doi.org/10.1021/acsomega.3c00874

[24] Castaneda FD, Garcia-Acosta G, Garzon-Alvarado D, *et al*. Design for the additive manufacturing of structural elements with cellular materials using Voronoi diagrams and Delaunay triangulations: Biological and structural applications. *Mechanics of Advanced Materials and Structures* 2023, 1–21. https://doi.org/10.1080/15376494.2023.2276837

[25] Xu Y, Pan H, Wang R, *et al*. New families of triply periodic minimal surface-like shell lattices. *Additive Manufacturing* 2023, **77**: 103779. https://doi.org/10.1016/j.addma.2023.103779

[26] Shevchenko AP, Shabalin AA, Karpukhin IY, *et al*. Topological representations of crystal structures: generation, analysis and implementation in the TopCryst system. *Science and Technology of Advanced Materials: Methods* 2022, **2**: 250–265. https://doi.org/10.1080/27660400.2022.2088041

[27] nTop Documentation, Release 4.0, https://support.ntop.com/hc/en-us/articles/360055403953-How-to-build-a-customlattice-unit-cell

[28] Blatov VA. A method for topological analysis of rod packings. *Structural Chemistry* 2016, **27**: 1605–1611. https://doi.org/10.1007/s11224-016-0774-1

[29] Blatov VA, Delgado-Friedrichs O, O'Keeffe M, *et al*. Threeperiodic nets and tilings: natural tilings for nets. *Acta Crystallographica Section A* 2007, **63**: 418–425. https://doi.org/10.1107/S0108767307038287

[30] Fischer W, Koch E. New surface patches for minimal balance surfaces. I. Branched catenoids. *Acta Crystallographica Section A* 1989, **45**: 166–169. https://doi.org/10.1107/S0108767388010797

[31] Porous 3D Documentation, Release 1.0.1, https://p3d.topcryst.com/software/

[32] Cohen-Steiner D, Morvan JM. Restricted Delaunay triangulations and normal cycle. In: SCG '03 Proceedings of the nineteenth annual symposium on Computational geometry, 2003: 312–321. https://doi.org/10.1145/777792.777839.

[33] Schoen AH. Reflections concerning triply-periodic minimal surfaces. *Interface Focus* 2012, **2**: 658– 668. https://doi.org/10.1098/rsfs.2012.0023.

[34] Brakke KA. The Surface Evolver. *Experimental Mathematics* 1992, **1**: 141–165. https://doi.org/10.1080/10586458.1992.10504253

[35] Shevchenko V, Balabanov S, Sychov M, et al. Prediction of Cellular Structure Mechanical Properties with the Geometry of Triply Periodic Minimal Surfaces (TPMS). *ACS Omega* 2023, **8**: 26895–26905. https://doi.org/10.1021/acsomega.3c01631

[36] Top N, Sahin I, Gokce H. The Mechanical Properties of Functionally Graded Lattice Structures Derived Using ComputerAided Design for Additive Manufacturing. *Applied Sciences* 2023, **13**: 11667. https://doi.org/10.3390/app132111667

[37] Khaleghi S, Baghani M, Karimpour M, *et al*. Novel modified triply periodic minimal surfaces (MTPMS) developed using genetic algorithm. *Journal of Materials Research and Technology* 2023, **26**. https://doi.org/10.1016/j.jmrt.2023.08.040

[38] Formalev VF. *Thermal conductivity of anisotropic bodies. Analytical methods for problem solving*. Moscow (Russia): Fizmatlit, 2015.

[39] Kanit T, Forest S, Galliet I, *et al*. Determination of the size of the representative volume element for random composites: statistical and numerical approach. *International Journal of Solids and Structures* 2003, **40**: 3647–3679. https://doi.org/10.1016/S0020-7683(03)00143-4

[40] Epov MI, Terekhov VI, Nizovtsev MI, *et al*. Effective thermal conductivity of dispersed materials with contrast inclusions. *High Temperature* 2015, **53**: 45–50. https://doi.org/10.1134/S0018151X15010046

[41] Prajapati H, Ravoori D, Woods RL, *et al*. Measurement of anisotropic thermal conductivity and interlayer thermal contact resistance in polymer fused deposition modeling (FDM). *Additive Manufacturing* 2018, **21**: 84–90. https://doi.org/10.1016/j.addma.2018.02.019

[42] Elkholy A, Rouby M, Kempers R. Characterization of the anisotropic thermal conductivity of additively manufactured components by fused filament fabrication. *Progress in Additive Manufacturing* 2019, **4**: 497–515. https://doi.org/10.1007/s40964-019-00098-2

[43] Scholz G, Gehringer M. *Thermoplastic Elastomers: At a Glance*. Boston (USA): De Gruyter, 2021. https://doi.org/10.1515/9783110739848

Acknowledgements

The research was supported by the Russian Science Foundation (grant No. 22– 23–00300).

Author contributions

Anton V. Eremin is responsible for Conceptualization (Equal), Data curation (Equal), Formal analysis (Equal), Funding acquisition (Lead), Investigation (Equal), Methodology (Equal), Project administration (Equal), Supervision (Equal), Writing - original draft (Equal), Writing - review & editing (Equal); Mikhail A. Frolov is responsible for Conceptualization (Equal), Data curation (Equal), Formal analysis (Equal), Investigation (Equal), Methodology (Equal), Validation (Equal), Writing - original draft (Equal), Writing - review & editing (Equal); Alexander F. Krutov is responsible for Conceptualization (Equal), Data curation (Equal), Formal analysis (Equal), Investigation (Equal), Methodology (Equal), Project administration (Equal), Supervision (Equal), Validation (Equal), Writing - original draft (Equal), Writing - review & editing (Equal); Mikhail I. Smolkov is responsible for Conceptualization (Equal), Data curation (Equal), Formal analysis (Equal), Investigation (Equal), Methodology (Equal), Resources (Equal), Software (Lead), Validation (Equal), Visualization (Equal), Writing - original draft (Equal), Writing - review & editing (Equal); Dmitry M. Bragin is responsible for Conceptualization (Equal), Data curation (Equal), Formal analysis (Equal), Investigation (Equal), Methodology (Equal), Validation (Equal), Visualization (Equal), Writing - original draft (Equal), Writing - review & editing (Equal); Andrey I. Popov is responsible for Conceptualization (Equal), Data curation (Equal), Formal analysis (Equal), Investigation (Equal), Methodology (Equal), Validation (Equal), Visualization (Equal), Writing - original draft (Equal), Writing - review & editing (Equal). All the authors have approved the final manuscript.

Declaration of competing interest

The authors have no competing interests to declare that are relevant to the content of this article.

Data availability statement

The data that support the findings of this study is available from the corresponding author upon reasonable request.

Use of AI statement

None.

Author biography

Anton Vladimirovich Eremin. Doctor of Engineering Sciences. Head of Heat Power Department and Vice-Rector for Integration Projects, Samara State Technical University. Research interests: computational methods, thermodynamics.

Mikhail Alexandrovich Frolov. Candidate of Engineering Sciences, Assistant Professor of Department of General and Inorganic Chemistry, Engineer of Samara Center of Theoretical Materials Science, Samara Polytech, Samara, Russia. Research interests: chemistry, physics, and materials mechanics, continuum mechanics.

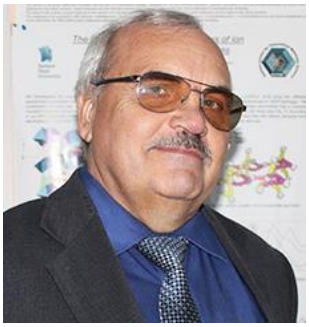

Alexander Fedorovich Krutov. Doctor of Physical and Mathematical Sciences, professor, Head of Laboratory of Computational Geometry and Theoretical Materials Science, PSUTI, Senior Research Officer of Samara Center of Theoretical Materials Science, Samara Polytech, Samara, Russia. Research interests: mathematical physics, relativistic theory of composite systems, theory of functional electron density, theoretical materials science.

Mikhail Igorevich Smolkov. Candidate of Physical and Mathematical Sciences degree seeking applicant, Research assistant of Laboratory of Computational Geometry and Theoretical Materials Science, PSUTI, Research Officer of Samara Center of Theoretical Materials Science, Samara Polytech, Samara, Russia. Research interests: computational geometry, computational mathematics, programming, machine learning.